First-principles study of structural, electronic, elastic and optical properties of alkali lead iodides $MPbI_3$ (M = Li, Na, K)

[1] Hameed T. Abdulla and [2] Sarkawt A. Sami

[1] Department of Physics, Faculty of Science, University of Zakho, Kurdistan Region, Iraq hameed.abdulla@uoz.edu.krd
[2] Department of Physics, College of Science, University of Duhok, Kurdistan Region, Iraq sarkawt@uod.ac

Received: 30.08.2022

Abstract. Inorganic halide-based perovskites are of great interest as materials for photo-voltaic and optoelectronic devices. Here we present a first-principles study of the structural, electronic, elastic and optical properties of alkali-metal lead iodides $MPbI_3$ (M = Li, Na, K), with the emphasis on the role of their first cation M. In particular, this work is the first investigation of the elastic and optical properties of $MPbI_3$ (M = Na, K). Our results show that the first cation has insignificant effect on the properties mentioned above, although there is some increase in the lattice constant when we pass from Li to Na. The energy band gap values calculated for our perovskites in a generalized gradient approximation agree with the available theoretical data but not with the experimental results. A better agreement with the experiment can be achieved with the approaches of Green's function and screened Coulomb interaction approximation. We demonstrate that our compounds have a direct band gap. The optical properties of $MPbI_3$ are calculated using a density-functional perturbation theory. Our data shows that $MPbI_3$ (M = Na, K) have a weak response to electromagnetic radiation at high photon energies and a strong response at low energies.

Keywords: perovskites, structure, elastic properties, optical properties, density-functional theory, energy gap, density of states.

UDC: 535.3

1. Introduction

In the past decade, perovskite-based solar cells have become one of the most significant energy sources which prevent the power industry from the crisis equivalent to global warming. The problems of environmental pollution have motivated the researchers in the field to search for environmentally friendly and low-consumption energy sources as an alternative to traditional ones. The perovskite solar cells are promising in a photovoltaic world because of their low-cost fabrication, easy manufacturing and outstanding optoelectronics and photovoltaic properties [1–4]. The general chemical formula of a perovskite is ABX_3, where A denotes an organic/inorganic cation, B a metal cation, and X a halide anion bonded to both cations. The progress in the efficiency of the perovskite solar cells has started from 3.8% in 2009 [5] and reached 25.2% in 2018 [6]. This has made these cells popular for multi-scale applications, including such photovoltaic and optoelectronic devices as field-effect transistors [7], laser diodes, γ-ray detectors, photodetectors and light emitting diodes [8–12]. Despite a rapid efficiency increase for the perovskite solar cells in the recent decade, the current records for their power-conversion efficiency still fall behind the radiative limit called a Shockley–Queisser limit, which is attributed to the non-radiative recombination losses [13–15].

Halide perovskite materials (see Refs. [16, 17]) have also gained a great attention due to their high photo-conversion efficiency. The photovoltaic properties of organic–metal–halide (organic–inorganic) perovskites facilitate many interesting applications. Their peculiar features such as a reduced intrinsic recombination, a suitable band gap, a high absorption coefficient and a stable mobility of electrons and holes are the causes of high photo-conversion efficiency of the corresponding solar cells [18–22]. In 2011, the photo-conversion efficiency 23.7% has been reported for a methylammonium lead iodide ($MAPbI_3$) perovskite [23].

Numerous varieties of this class of the perovskite solar cells have been offered through changing organic cations and halide anions [24–26], with a chemically stable composition. Inorganic halide perovskites have also been developed since these they are considered to have an excellent chemical stability [27]. This contrasts with most of the organic–inorganic halide perovskites for which a problem of chemical instability is well known. The energy conversion efficiency higher than 10% has been obtained basing on $CsPbI_3$-perovskite solar cells [28]. The replacement of Pb by Sn in the $CsPbX_3$-type compounds has been widely studied due to toxicity of Pb [29].

Replacement of any atom in the crystal structure of perovskites cause changes in their electronic and optical properties (see, e.g., Ref. [30]). This concerns both cations and anions. In addition to the changes in the properties of perovskites, the bond lengths are affected by the change in cation sizes [31]. The structural parameters of the above compounds are also influenced by the replacement of any atom from the same group. The inorganic lead perovskite $APbI_3$ with the cations A = Li, Na, K and Cs have been studied experimentally by Dimesso et al. [32]. It has been predicted that the cation size affects only slightly the band gap. Perovskites $CsPbX_3$ with X = Cl, Br and I have been investigated under hydrostatic pressure [33]. Small pressure-driven changes in their properties have been found, as well as the changes associated with anionic substitutions. A different anion means a change in the relative electro-negativity between an anion (X) and a cation (B), which leads to changing lattice constant, band structure, energy gap and some other properties.

Almost a decade ago, a number of high-quality reviews have been published on the materials mentioned above [4, 28, 34–38]. Note that organic perovskites have already become the most important materials which manifest a high enough solar-cell efficiency in the past 8 years. However, due to their hygroscopic and volatile nature, they suffer from chemical instability, in particular at high temperatures. Therefore, inorganic perovskites are emerging as their efficient alternatives. This is also because of their unique properties such as a tunable bandgap and a strong emission.

Inorganic perovskites are the main materials of many commercial perovskite-based solar cells owing to their excellent thermal stability and optimized power-conversion efficiency (up to 19% – see Ref. [39]). A narrow band gap of the inorganic perovskites should imply some opportunities for improving further their efficiency. As follows from the advantages highlighted above, these perovskites are now attracting a great attention as promising materials for future applications. Understanding the opto-electronic properties of perovskites is crucial to predict their behaviour. In its turn, these predictions are essential to engineer perovskites for different applications. Among these properties, the refractive index and the energy band gap are of primary importance.

The electronics structure of $APbI_3$ and $APbBr_3$, with A denoting Li, Na, K, Rb and Cs, has been calculated by Pitriana et al. [40, 41]. However, the optical and elastic properties have not been dealt with there. In the present work, we study theoretically the structural, electronic, elastic and optical properties of inorganic alkali lead iodides $MPbI_3$ (M = Li, Na, K), using ab initio calculations. In particular, we calculate a Kohn–Sham gap in the frame of a known Perdew–Burke–Ernzerhof generalized gradient approximation (PBE-GGA). Moreover, we employ Green's function and screened Coulomb-interaction (GW) approximations to correct the fundamental band gap, which thus becomes more compatible with the experimental E_g values.

2. Computational details

All of our calculations for $MPbI_3$ have been conducted for the ambient pressure and temperature. Our first-principles study is performed within the framework of a density-functional theory, using a known Abinit software package [42]. In the calculations, the exchange-correlation functional is processed with the GGA approach which utilizes a 'flavour' of the PBE approach [43]. This approach considers the states $1s^2 2s^1$ for Li, $2s^2$, $2p^6$ and $3s^1$ for Na, $3s^2$, $3p^6$ and $4s^1$ for K, $5d^{10}$, $6s^2$ and $6p^2$ for Pb, and $5s^2$ and $5p^5$ for I as the valence states [44]. The norm-conserving pseudopotential by Goedecker, Teter and Hutter has been used [45]. The space group of the cubic phase of ABX_3 is $Pm\overline{3}m$ (#221). The cubic structure of perovskites involves five atoms per primitive cell. The unit cell of the crystal contains one atom of Li, Na and K, one atom of Pb and three atoms of I. The A atom which represents Li, Na or K is located at the position (0.0, 0.0, 0.0), the B atom (i.e., Pb) at (0.5, 0.5, 0.5), and the three X atoms representing I at (0.0, 0.5, 0.5), (0.5, 0.0, 0.5) and (0.5, 0.5, 0.0).

First, optimization of the crystal structure is done for $MPbI_3$ in its cubic-phase structure. The lattice constant, the unit-cell volume and the total energy are calculated. Second, the convergence procedure is applied to the main input variables, namely the cut-off energy (the e-cut) and the k-point mesh. The number of plane waves at a given k point is controlled by the e-cut. The condition of convergence predicts the most suitable e-cut value and the k-point mesh size. In our calculations, the convergence has given the e-cut and the k-points to be equal to 1088 eV and the sampling Brillouin zone 8×8×8, respectively based on the Monkhorst–Pack approach [46], respectively. The atomic coordinates and the lattice constant have been the basis for calculating the band structure and then the energy gap, using the GGA within the PBE approach. The GW approximation has been utilized in order to correct the energy band gap.

The optical properties of $MPbI_3$ have been calculated using the Abinit code, which implements the Kramers–Kronig relations [47], and the density-functional perturbation theory [48]. The imaginary and real parts of the dielectric function are computed based upon the expression derived from the density-functional perturbation theory. In addition to the dielectric function, the absorption coefficient and the refractive index have been calculated for examining the response of our compounds to visible light. The calculations of the optical properties require a denser set of the k-points and, therefore, the mesh 24×24×24 has been used. The calculations for $CsPbI_3$ have been carried out prior to the calculations for $MPbI_3$. The lattice constant a of $CsPbI_3$ is equal to 6.242 Å, which agrees with the parameter calculated in Ref. [49], while the unit-cell volume is 252.91 $Å^3$. The energy band gaps obtained with the Kohn–Sham approach and the GW approximation amount respectively to 1.38708 eV and 2.095 eV. The Cs–I and Pb–I bond lengths are equal respectively to 4.47175 Å and 3.16201 Å. These parameters agree well with the calculation data reported in Ref. [50]. Then the same methodology and the same input variables have been used in the case of $MPbI_3$ compound.

3. Results and discussion

3.1. Structural properties

In any ab initio approach, the first and the most important step in the calculations of properties of a material is computing its structural parameters, which are fundamental for predicting the electronic, optical and elastic properties. In other words, the structural information on a given compound enables the calculations of its other properties. The three compounds studied in this work belong to the ABX_3-perovskite family. As stressed above, they can be considered to have the cubic crystalline structure described by the space group ($Pm\bar{3}m$) (#221). The crystal structure and the first Brillouin zone of cubic $MPbI_3$ (M = Li, Na, K) are shown in Fig. 1. The M atom is located at the corner of the unit cell with the fractional coordinates (0.0, 0.0, 0.0), the Wyckoff site *1a*, and the site symmetry ($m\bar{3}m$). The body-centred position is occupied by Pb atom, with the fractional coordinates (0.5, 0.5, 0.5), the Wyckoff site *1b* and the site symmetry ($m\bar{3}m$). Finally, the positions of I atoms are face-centred, with the fractional coordinates (0.0, 0.5, 0.5), (0.5, 0.0,0.5) and (0.5, 0.5, 0.0), the Wyckoff site *3c*, and the site symmetry (4/mm. m).

The unit cell parameters, including the lattice constant, the total energy and the unit-cell volume, the bulk modulus and the pressure derivative obtained for $MPbI_3$ after optimization are displayed in Table 1. The calculated structural parameters are in a good agreement with the available data of the earlier theoretical works. Dependences of the total energy on the lattice constant for the three compounds are plotted in Fig. 2. Note that the lattice constants are chosen in the minimum point of the total energy. Some difference among the results of the present calculations and those of the literature can be due to the different types of pseudo-potentials and the software packages used. One can also notice that the lattice constant slightly increases depending on the size of the cation in the sequence Li, Na and K (see Fig. 3a). A similar small change is also observed in the bond length (see Fig. 3b). This confirms an insignificant effect of the first cation on the structure.

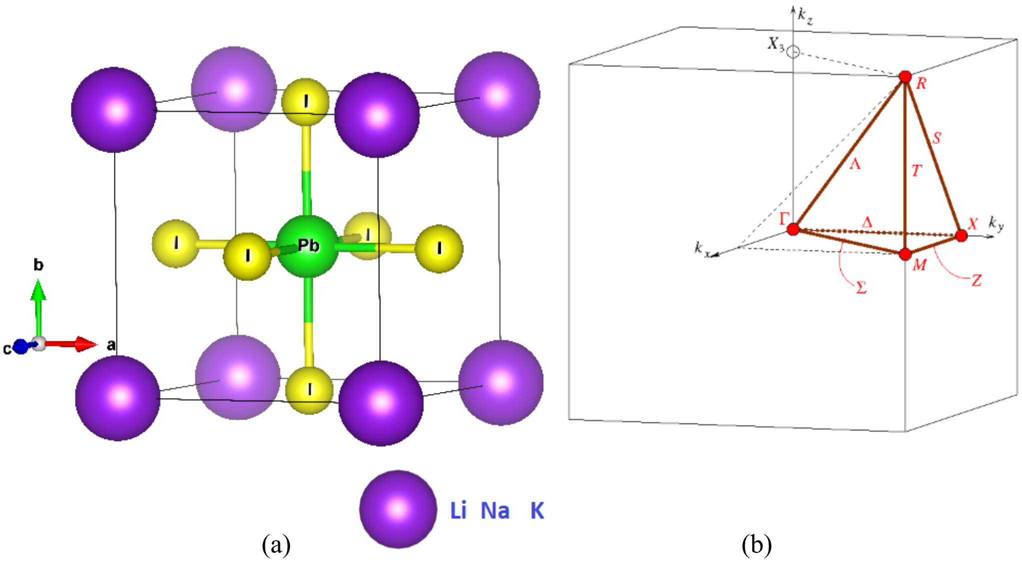

(a) (b)

Fig. 1. Crystal structure of cubic $MPbI_3$ (M= Li, Na, K) (a) and its first Brillouin zone that involves high-symmetry points and lines (b).

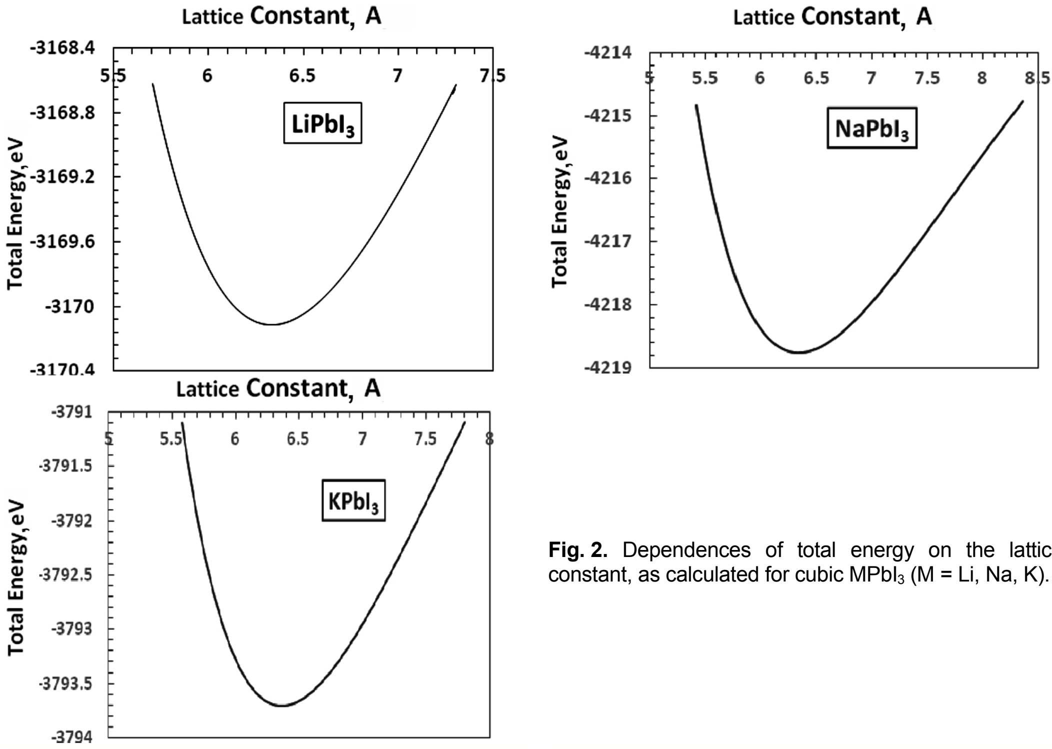

Fig. 2. Dependences of total energy on the lattice constant, as calculated for cubic $MPbI_3$ (M = Li, Na, K).

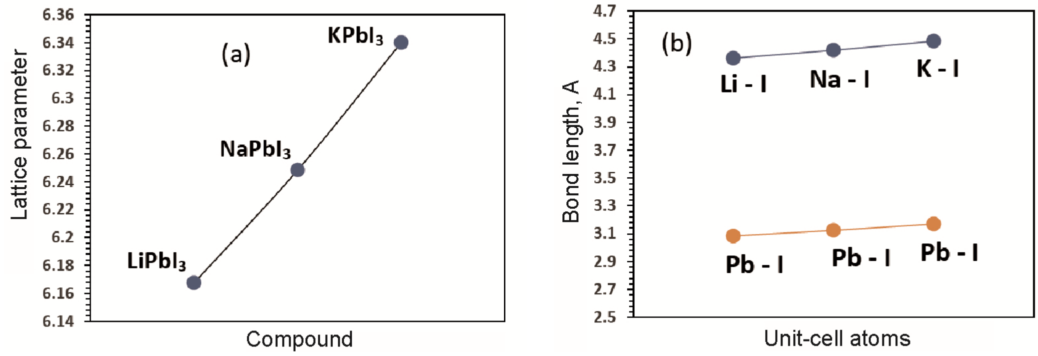

Fig. 3. Variation of a lattice constant for $MPbI_3$ (M = Li, Na, K) (panel a) and dependence of bond length on the changing size of the first cation (panel b).

The effect of pressure P on the volume V of the unit cell is shown in Fig. 4. The data can be fitted with the second-order Birch–Murnaghan equation [51, 52]:

$$P = \frac{3}{2}B_0\left[\left(\frac{V_0}{V}\right)^{7/3} - \left(\frac{V_0}{V}\right)^{5/3}\right]\left[1 + \frac{3}{4}\left(B_0^{'} - 4\right)\left\{\left(\frac{V_0}{V}\right)^{2/3} - 1\right\}\right], \tag{1}$$

where B_0 and $B_0^{'}$ are respectively the bulk modulus and its first derivative with respect to the pressure, and V_0 denotes the unit-cell volume. Note that all the parameters are taken at a zero pressure. From the fitting, the bulk modulus and its derivative have been calculated for the three compounds (see Table 1 where the other results available in the literature are also shown). The bond length for $MPbI_3$ (M = Li, Na, K) has been calculated using the PBE–GGA optimization. It is seen from Table 1 that the Pb–I-bond length agrees well with the other available data. Unfortunately, the literature results needed to make comparisons for the others bonds are absent.

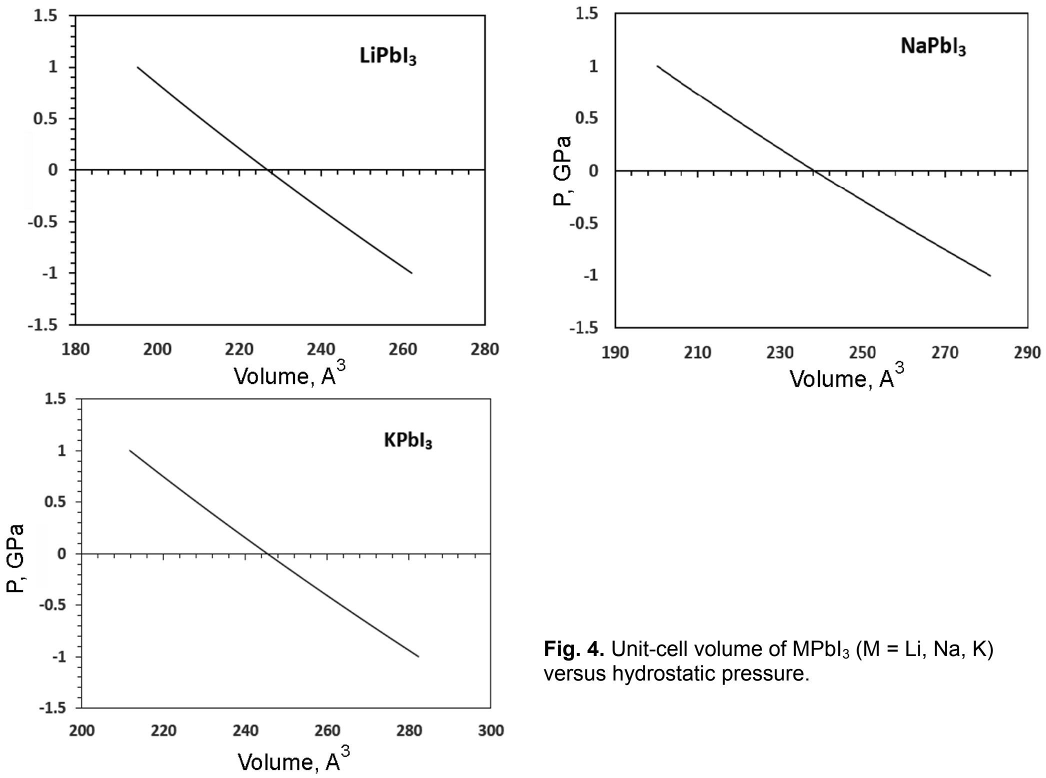

Fig. 4. Unit-cell volume of MPbI$_3$ (M = Li, Na, K) versus hydrostatic pressure.

Table 1. Lattice constant a, total energy E_T, bond energy E_b, unit-cell volume V, bulk modulus B_0 and its pressure derivative $B_o^{'}$ calculated for MPbI$_3$ compounds (M = Li, Na, K).

Compound	Calculated parameter	Present work	Other works	Experimental result
LiPbI$_3$	a, Å	6.16750	6.1978 [53] 6.321 [54] 6.0057 [55]	n. a.
	E_T, eV	–3169.63	n. a.	n. a.
	E_b, eV	–362.51	n. a.	n. a.
	V, A^3	234.59	n. a.	n. a.
	B_0, GPa	16.9382	17.417 [53]	n. a.
	$B_0^{'}$	4.8099	4.49 [53]	n. a.
NaPbI$_3$	a, Å	6.24850	6.331 [54]	n. a.
	E_T, eV	–4218.62	n. a.	n. a.
	E_b, eV	–524.47	n. a.	n. a.
	V, A^3	243.9	n. a.	n. a.
	B_0, GPa	16.9304	n. a.	n. a.
	$B_0^{'}$	4.4126	n. a.	n. a.
KPbI$_3$	a, Å	6.33999	6.352 [54]	n. a.
	E_T, eV	–3793.67	n. a.	n. a.
	E_b, eV	401.92	n. a.	n. a.
	V, Å^3	254.83	n. a.	n. a.
	B_0, GPa	14.8642	n. a.	n. a.
	$B_0^{'}$	5.0248	n. a.	n. a.

* Here and below the notation “n. a.” stands for “not available”.

Table 2. Bond lengths for $MPbI_3$ (M = Li, Na, K), as calculated from the PBE–GGA optimization.

Compounds	Bond	Bond length, Å		
		Present work	Theoretical	Experimental
$LiPbI_3$	Li (1) – I (3)	4.36108	n. a.	n. a.
	Pb (2) – I (3)	3.08375	n. a.	3.18 [56]
$NaPbI_3$	Na (1) – I (3)	4.41835	n. a.	n. a.
	Pb (2) – I (3)	3.12425	n. a.	3.18 [56]
$KPbI_3$	K (1) – I (3)	4.48305	n. a.	n. a.
	I (3) – Pb (2)	3.16999	n. a.	3.18 [56]

3.2. Electronic properties

The calculations of the band structure and the total and partial densities of electronic states have revealed the electronic properties of $MPbI_3$ (M = Li, Na, K). Fig. 5 shows the electronic band structures of the three compounds. The red dashed line denotes the Fermi level E_f, i.e. the highest occupied electronic state. All of the compounds manifest a direct fundamental band gap E_g occurring between the bands 22 and 23 (22 and 23 bands are the n-band numbers of the more than 50 bands used in our calculations) at the symmetry point R. The E_g values calculated for $LiPbI_3$, $NaPbI_3$ and $KPbI_3$ are displayed in Table 3.. These values agree well with the available theoretical data. In spite of this fact, our results do not agree too well with the experimental data.

Table 3. Kohn–Sham gaps and fundamental band gaps calculated for our perovskites.

Compound	Kohn–Sham gap, eV (PBE–GGW)		Fundamental band gap, eV		
	Present work	Other works	Present work	Experimental	Theoretical
$LiPbI_3$	1.41336	1.403 [53] 1.43 [41] 1.45 [55]	2.2	2.36 [32]	n. a.
$NaPbI_3$	1.39501	1.48 [37]	2.1	2.30 [32]	n. a.
$KPbI_3$	1.41494	1.36 [37]	2.116	2.19 [32] 2.2 [57]	n. a.

A typical problem of reduced gap obtained from the density-functional theory, if compared with the experiments, has found a number of solutions. We have used the GW approximation to compute the E_g parameter more accurately. It is seen from Table 3 that the GW-calculated E_g values are more compatible with the experimental results. A small difference in the shapes of the electronic band structures for different compounds is, of course, attributed to different first cations (Li, Na and K). The degeneracy of the bands 22 and 23 is essential because they accommodate more possibilities for the excitation of electrons from the valence band (VB). This leads to a good response of our compounds to electromagnetic excitations. In addition to the fundamental band gap at the point R of the Brillouin zone, Table 4 shows the direct band gaps E_g calculated at the other high-symmetry points Γ, X and M.

We remind again that our perovskites represent semiconductors with a direct fundamental band gap at the symmetry point R. As far as the authors know, there is neither theoretical nor experimental literature E_g data at the high-symmetry points Γ, X and M of our compounds, which could be used for comparison. Nonetheless, the values of the fundamental energy band gaps derived by us indicate that our compounds are indeed semiconductors. Moreover, the fundamental gap between the top of the VB and the bottom of the conduction band (CB) is indeed located at the symmetry point R. Finally, we note that the band gap of any optical material is of a primary importance since it affects directly the power-conversion efficiency of the solar cells and the other photovoltaic devices.

Table 4. Energy band gaps calculated for our perovskites at some symmetry points, using the PBE–GGA approach.

Compound	$E^{\Gamma-\Gamma}$, eV	E^{X-X}, eV	E^{M-M}, eV	E^{R-R}, eV
$LiPbI_3$	2.90697	2.96316	2.29689	1.41336
$NaPbI_3$	2.95354	2.96336	2.25418	1.39501
$KPbI_3$	3.74599	3.08288	2.30203	1.41494

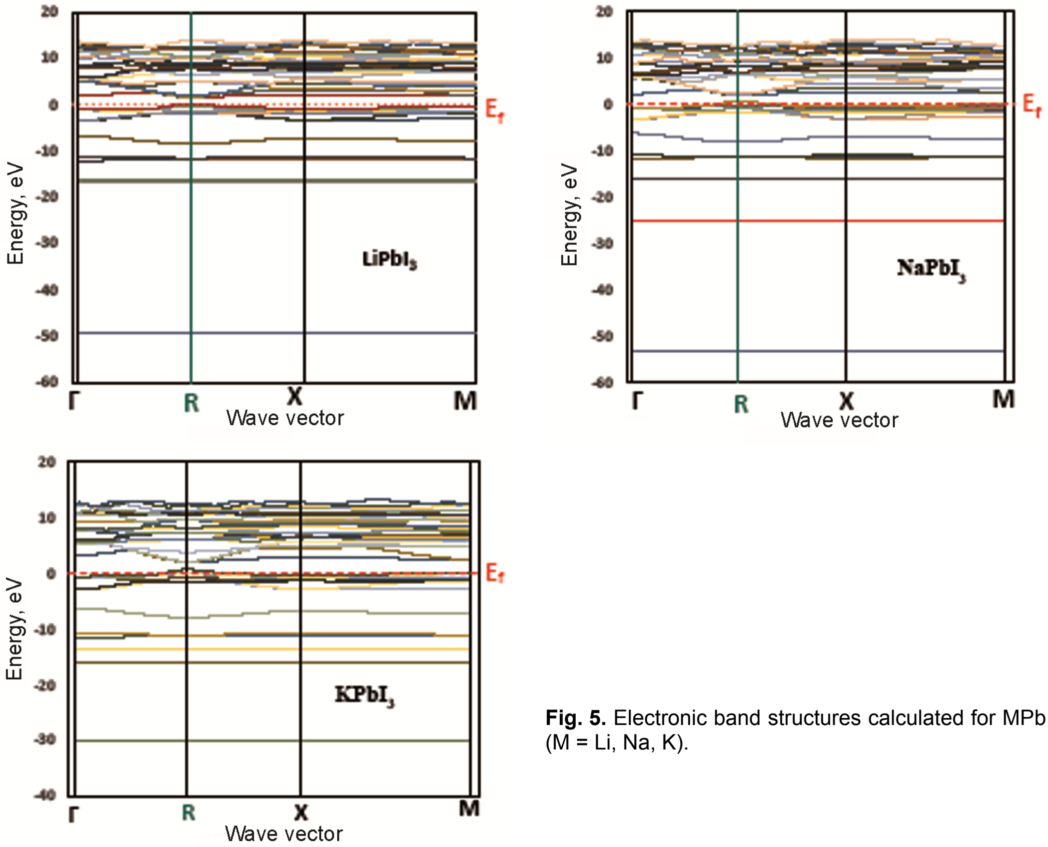

Fig. 5. Electronic band structures calculated for $MPbI_3$ (M = Li, Na, K).

To understand better the electronic properties of $MPbI_3$ (M = Li, Na, K), we have calculated the total and partial densities of the electronic states, using the GGA–PBE method. These characteristics are shown in Fig. 6. The most significant contributions to the densities of states for the three perovskites are located between the Fermi-level energy and –3 eV. Inside the VB, a large contribution for $NaPbI_3$ and $KPbI_3$ is seen at –16 eV and a smaller one corresponds to –11 eV (see Fig. 6e and Fig. 6f). On the other hand, an essential contribution for $LiPbI_3$ occurs at –11 and –12 eV (see Fig. 6d). Inside the CB, the contributions into the density of states are seen between 1.5 eV and less than 14 eV for $LiPbI_3$ (Fig. 6d) and from 2 eV to almost 14 eV for $NaPbI_3$ (Fig. 6e). In the case of $KPbI_3$, the electronic states are seen from 2 eV to 13 eV (Fig. 6f).

The plots in the left panel of Fig. 6 show the partial density of states for the $MPbI_3$ compounds (M = Li, Na, K). As seen from Fig. 6a, the VB for $LiPbI_3$ includes a high contribution of the I–5*s* state (at –13 eV), with a less participation of the Li–1*s* (at –50 eV) and Pb–6*s* (from –7 to –9 eV) states. The I–5*p* state has a large contribution from E_f to – 3 eV and an extremely small one from E_f to –50 eV. A contribution of the Li–2*s* state is observed between 5 eV to 14 eV in the CB, with a smaller participation of I–5*p*. The Pb–6*p* state is located near E_g and its participation is insignificant. Finally, a mixture of the I–5*s*, I–5*p*, Li–2*s* and Pb–6*p* states gives rise to the CB.

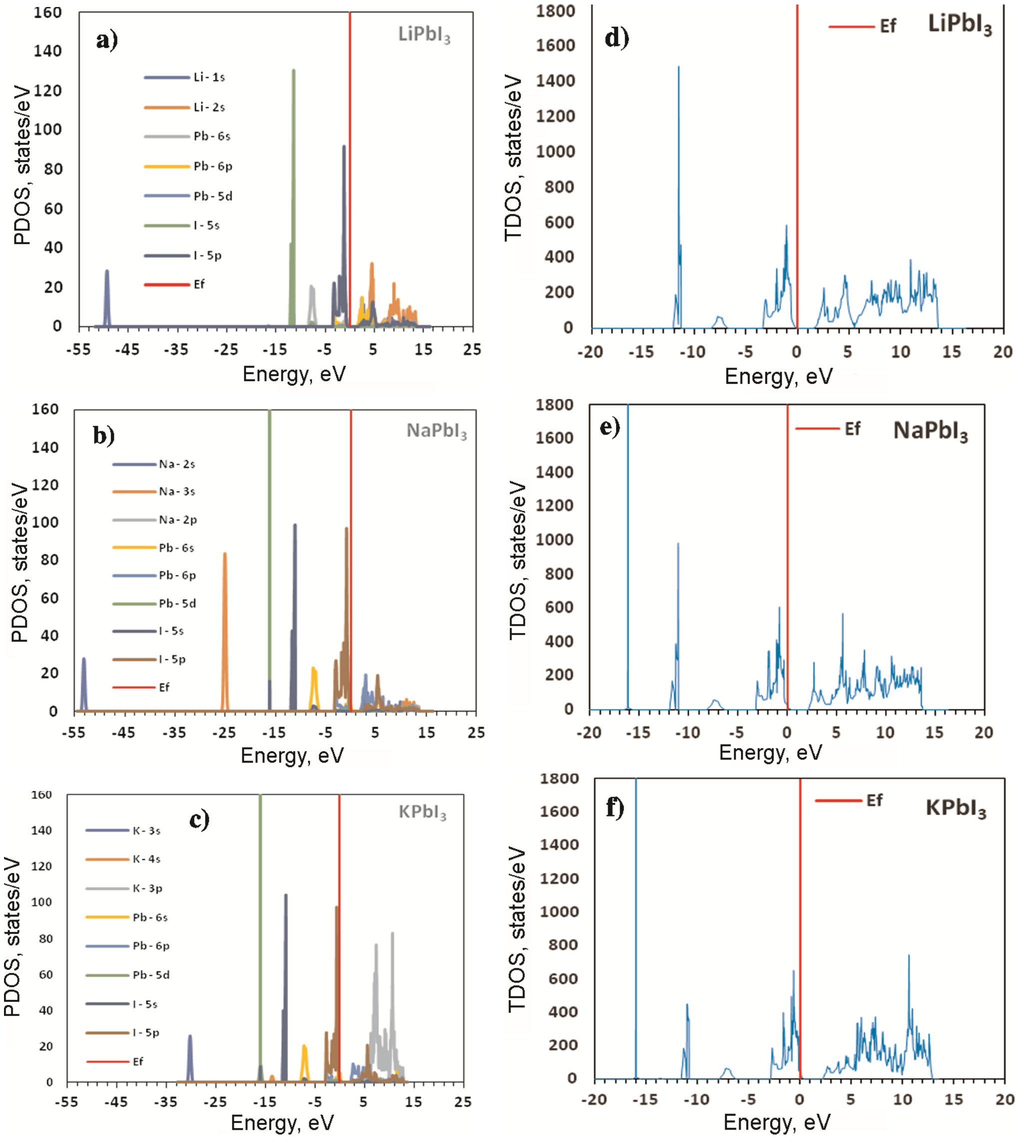

Fig. 6. Partial (left panels) densities of states for $LiPbI_3$ (a), $NaPbI_3$ (b) and $KPbI_3$ (c) and total (right panels) densities of states for $LiPbI_3$ (d), $NaPbI_3$ (e) and $KPbI_3$ (f).

The partial density of states for the $NaPbI_3$ compound is shown in Fig. 6b. Here the Pb–5*d* state has a high contribution into the VB at –14 eV. The Na–2*s* and Pb–6*s* states reveal small contributions at –53 eV and –7 eV, respectively. In addition, large contributions of the I–5*p*, I–5*s* and Na–3*s* states can be observed in the VB, though at different energies. The CB of $NaPbI_3$ shows a high contribution of the Na–3*s* and Pb–6*p* states and a less participation of the Na–3*s* state. On the whole, the CB is formed due to the Pb–6*p*, I–5*s*, Na–3*s* and I–5*p* states.

The partial density of states for $KPbI_3$ is shown Fig. 6c. Here the I–5*s* and I–5*p* states notably contribute respectively at –11 eV and near E_f, while the participation of the Pb–5*d* state at –16 eV is more serious. The K–3*s* and Pb–6*s* states participate less in the band formation (see Fig. 6c). On the other hand, the K–3*p* state controls the CB from 5 eV to 14 eV. Furthermore, there is small contribution of the I–5*p* state into the band. The Pb–6*p* state participates in the formation of the CB with a very small expanse near E_g, in addition to a weak contribution from the Pb–6*p* state in the VB, which is mixed with the I–5*s* and I–5*p* states.

3.3. Elastic properties

The elastic constants are fundamental in the description of mechanical properties of any material. In this work we have calculated the elastic constants C_{11}, C_{12} and C_{44} for our $MPbI_3$ compounds (M = Li, Na, K). They can be used for determining the Young's modulus *Y*, the shear modulus *G*, the bulk modulus *B*, the Pugh's ratio *B*/*G*, the Poisson's ratio *v*, and the strength of our materials. The Pugh's ratio determines the brittleness or elasticity of the materials [58]. A small/large *B*/*G* value is associated with a brittle/ elastic material. The elastic constants provide a valuable information on the structural stability and mechanical properties of a material. Under the conditions of linear elastic deformation, one can use the Hook's law to describe solid bodies. Its usual form is as follows:

$$\sigma_{ij} = \sum_{kl} C_{ijkl}\,\epsilon_{kl}\,, \tag{2}$$

where C_{ijkl} are the second-order elastic constants [59], i, j, k, $l = 1, 2, 3$, ϵ_{kl} are the strain components and σ_{ij} the stresses. The elastic constants can be evaluated using the stress–strain relationship based on the calculations of the total energy E_{tot}. The second-order elastic constants are related to the E_{tot} parameter of a crystal through the Taylor expansion in terms of the strain components truncated to the second order:

$$E\left(V,\epsilon\right)=E\left(Vo\right)+V\sum_{\alpha}\sigma_{\alpha}\,\epsilon_{\alpha}\;\frac{V}{2}\sum_{\alpha\beta}C_{\alpha\beta}\epsilon_{\alpha}\epsilon_{\beta}\,, \tag{3}$$

where V_0 is the equilibrium volume and the Voigt notation is used (α, β = 1, 2, ….. 6) [60]. According to Eq. (3), the second-order elastic constants are related to the second strain derivatives of the E_{tot} parameter [61]:

$$C_{\alpha\beta} = \frac{1}{V}\frac{\partial^2 E}{\partial\epsilon_{\alpha}\,\partial\epsilon_{\beta}}\,. \tag{4}$$

For the cubic crystals, each of these independent elastic constants represents a directionally dependent mechanical response of a crystal for different directions of mechanical forces. Therefore, comprehensive understanding of the elastic constants and knowledge of their values is necessary for predicting the mechanical properties. Using the finite-strain theory, we have calculated the three elastic constants C_{11}, C_{12} and C_{44}. The elastic constants, the Cauchy pressure ($C_{12} - C_{44}$) [62] and the Zener anisotropy factor *A* [63] for $MPbI_3$ (M = Li, Na, K) are gathered in Table 5. The bulk modulus, the shear modulus, the Young's modulus, the Pugh's ratio and the Poisson's ratio are presented in Table 6. It is evident that the bulk modulus decreases when the first cation changes from Li to Na and then to K. The bulk modulus of $MPbI_3$ (M = Li, Na, K) calculated from C_{11}, C_{12} and C_{44} is close to that obtained from the fitting with the Birch–Murnaghan equation (see Table 1). The calculated bulk modulus of $LiPbI_3$ is in a good agreement with the theoretical result reported in Ref. [53]. This indicates that our calculation approach is reliable enough. Note also that the bulk modulus for $MPbI_3$ (M = Na, K) is not available for comparison. Then our results can motivate the future measurements. Due to different calculation methods, some discrepancies appear for the bulk moduli of $MPbI_3$ (M = Na, K) obtained by the Voigt–Reuss–Hill (VRH) averaging scheme [64] (see Table 6) and those obtained from the fitting with the Birch–Murnaghan equation (see Table 1).

Table 5. Elastic constants (in GPa), Cauchy pressure ($C_{12} - C_{44}$) and anisotropy factor calculated for $MPbI_3$ (M = Li, Na, K).

Compound	C_{11}	C_{12}	C_{44}	$C_{12} - C_{44}$	A
$LiPbI_3$	30.5	8.8	1.1	7.7	0.10
$NaPbI_3$	39.1	4.0	1.44	2.56	0.08
$KPbI_3$	32.3	3.2	1.3	1.9	0.09

Table 6. Bulk modulus B (in GPa), shear modulus G (in GPa), Young's modulus Y (in GPa), Pugh's ratio B/G and Poisson's ratio υ calculated for $MPbI_3$ (M = Li, Na, K) by the VRH scheme.

Compound parameter	$LiPbI_3$		$NaPbI_3$	$KPbI_3$
	Present work	Other works	Present work	Present work
B_V	16.02	17.417 [53]	15.66	12.90
G_V	5.02	n. a.	7.84	6.57
Y_V	13.64	n. a.	20.17	16.85
υ_V	0.35	n. a.	0.29	0.28
B_V/G_V	3.19	n. a.	1.99	1.96
B_R	16.02	n. a.	15.66	12.90
G_R	1.71	n. a.	2.17	2.00
Y_R	5.09	n. a.	6.22	5.71
υ_R	0.45	n. a.	0.43	0.43
B_R/G_R	9.36	n. a.	7.21	6.45
B_H	16.02	n. a.	15.66	12.90
G_H	3.39	n. a.	5.01	4.29
Y_H	9.50	n. a.	13.57	11.58
υ_H	0.40	n. a.	0.36	0.35
B_H/G_H	4.72	n. a.	3.12	3

* The subscripts *V*, *R* and *H* stand for the Voigt, Reuss and Hill schemes, respectively.

For the mechanical stability of crystals, the elastic constants should satisfy well-known Born stability criteria [65]. For the cubic structures, they look as follows:

$$C_{11} > 0,\ C_{44} > 0,\ C_{11} - C_{12} > 0,\ C_{11} + 2C_{12} > 0.$$

As seen from Table 5, our elastic constants satisfy the above criteria. The angular character of atomic bonding in a material could be characterized by a Cauchy pressure. If this pressure is negative, the material is expected to be non-metallic, with directional bonding. On the contrary, a positive Cauchy pressure indicates that the material is metallic [66]. It is clear from Table 5 that the Cauchy pressures for $MPbI_3$ (M = Li, Na, K) are positive, thus pointing to a metallic behaviour of our compounds. Note also that the Cauchy pressure for the $MPbI_3$ compounds decreases from Li to K. Moreover, a positive Cauchy pressure tells us that the material is highly elastic, while a negative one implies that it is brittle [62]. It is also important to investigate the Zener anisotropy factor which is a measure of anisotropy. A material is considered to be completely isotropic if we have $A = 1$, whereas a value larger or smaller than unity indicates some degree of elastic anisotropy. The A values calculated for $MPbI_3$ (M = Li, Na, K) are shown in Table 5. The A parameters are less than unity, which demonstrates that our perovskites are elastically anisotropic.

Note that the Zener anisotropy factor has been calculated as

$$A = \frac{2C_{44}}{\left(C_{11} - C_{12}\right)}. \tag{5}$$

The C_{11}, C_{12} and C_{44} parameters are independent for the cubic crystal systems. The longitudinal distortion C_{11} is associated with a longitudinal compression describing a hardness. The transverse distortion C_{12} is associated with a transverse expansion. It can be related to the Poisson's ratio. Finally, the shear modulus is based on the shear elastic parameter C_{44}. Issuing from the calculated C_{11}, C_{12} and C_{44} values, one can find such important parameters for the estimation of mechanical properties as the Young's modulus Y, the shear modulus G, the bulk modulus B and the Poisson's ratio v. They have been calculated for the $\mathrm{MPbI_3}$ (M = Li, Na, K) compounds, using the VRH averaging scheme. The Voigt- and Reuss-associated parameters (see the subscripts V and R) for the cubic systems are given by (see Ref. [67])

$$B_V = B_R = \frac{\left(C_{11} + 2C_{12}\right)}{3}, \tag{6}$$

$$G_V = \frac{C_{11} - C_{12} + 3C_{44}}{5}, \tag{7}$$

$$G_R = \frac{5C_{44}\left(C_{11} - C_{12}\right)}{\left[4C_{44} + 3\left(C_{11} - C_{12}\right)\right]}. \tag{8}$$

On the other hand, the shear and bulk moduli obtained with the Hill scheme read as

$$G = \frac{\left(G_V + G_R\right)}{2}, \tag{9}$$

$$B = \frac{\left(B_V + B_R\right)}{2}. \tag{10}$$

Finally, the following relations have been used to calculate the Poisson's ratio v and the Young's modulus Y:

$$v = \frac{3B - 2G}{2\left(3B + G\right)}, \tag{11}$$

$$Y = \frac{9GB}{3B + G}. \tag{12}$$

The Poisson's and Pugh's ratios are related to such mechanical properties of a material as ductility and brittleness. The critical Poisson's and Pugh's ratios that separate ductile and brittle materials are ~ 0.26 [68] and 1.75 [69], respectively. A material is considered as brittle if its Pugh's ratio is smaller than 1.75 and the Poisson ratio smaller than 0.26, while a ductile material has larger Pugh's and Poisson's ratios [70]. The bulk modulus represents a measure of resistance of a material to its deformation. The larger the bulk modulus, the stronger the resisting capacity of a material is. The Young's and shear moduli are considered to be measures of reversible resisting deformations with respect to the compression and shear stress, respectively. The Poisson's ratio is associated with stability of a material to the shear stresses and offers some details on the nature of its bonding forces [71]. More plasticity means a larger Poisson's ratio. The Poisson's ratio is smaller ($v \sim 0.1$) for covalent materials and larger ($v \sim 0.25$) for ionic materials. Finally, the forces in a solid material can be treated as central if the v value is between 0.25 and 0.50 [72].

Another way to separate ductile and brittle materials is the Frantsevich rule [73] for the Poisson's ratio: a material is ductile/brittle if its v value is larger/smaller than 1/3. It follows from the results obtained above and the Frantsevich rule that $\mathrm{LiPbI_3}$ should be treated as ductile. The

Poisson's and Pugh's ratios calculated for the $MPbI_3$ (M = Li, Na, K) compounds according to the VRH scheme are shown in Fig. 7. The overall variation of the Pugh's ratio due to structural changes is weak, and a similar situation approximately holds true for the Poisson's ratio of $NaPbI_3$ and $KPbI_3$. On the other hand, $LiPbI_3$ manifests the largest Poisson's ratio, which confirms its ductility. In addition, the Pugh's ratio increases slightly if one passes from K to Na and then to Li ion. In other words, our Poisson's and Pugh's ratios indicate that $LiPbI_3$ is a ductile material.

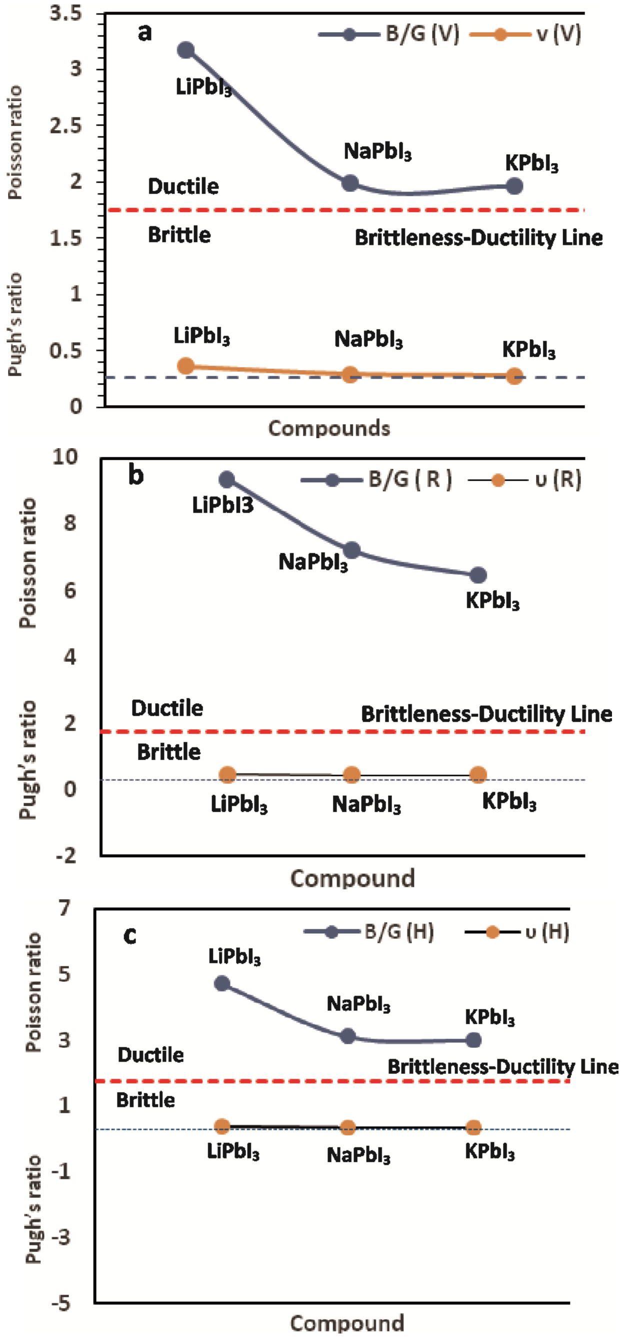

Fig. 7. Poisson and Pugh's ratios for $MPbI_3$ (M = Li, Na, K) calculated with the VRH scheme according to Voigt (a), Reuss (b) and Hil (c).

3.4. Optical properties

The optical properties describe a response of a material to electromagnetic radiation. To predict the optical behaviour, it would be essential to calculate the dielectric function because it describes both the electron–photon interactions and the propagation of electromagnetic waves in a given medium. We have studied such frequency-dependent characteristics of $MPbI_3$ (M = Li, Na, K) as the dielectric function, the absorption coefficient and the refractive index. To quantize the optical properties of a given material, it is convenient to employ its complex dielectric function $\varepsilon(\hbar\omega)$ ($\varepsilon = \varepsilon_1 + i\varepsilon_2$). Note that its real part is associated with the ability of a material to store electrical energy and polarize, while the imaginary part is linked with the energy loss and dissipation. The imaginary part of the dielectric function $\varepsilon_2(\hbar\omega)$ can be calculated as

$$\varepsilon_2 = \frac{2e^2\pi}{V\varepsilon_0}\sum_{K,v,c}\left|\left\langle\psi_K^c\middle|\hat{u}\cdot r\middle|\psi_K^v\right\rangle\right|^2\delta\left(E_K^c - E_K^v - \hbar\omega\right). \tag{13}$$

The Kramers–Kronig relation can be used to calculate the real part $\varepsilon_1(\hbar\omega)$ of the dielectric function:

$$\varepsilon_1 - 1 = \frac{2}{\pi}\int_0^\infty \frac{t\varepsilon_2(t)dt}{t^2 - (\hbar\omega)^2}. \tag{14}$$

The dielectric function can be found using the results for the electronic band structures. The imaginary parts of the dielectric functions calculated for $MPbI_3$ (M = Li, Na, K) are given in Fig. 8a. It is known that the imaginary part $\varepsilon_2(\hbar\omega)$ plays an important part for the optical transitions among unoccupied and occupied electronics states. One can notice that the appropriate peaks for the three perovskites are located in the visible region (around 3 eV), which implies a high optical absorption of the perovskites in the low-energy range. It is seen from Fig. 8a that the energy region 2.4–6.9 eV is a region of strong absorption of $MPbI_3$ (M = Li, Na, K). Furthermore, the information concerned with the transitions of electrons from the VB (the occupied states) to the CB (the unoccupied states) is given by lower-energy peaks. A number of critical points located at around 3.0, 3.5 and 3.8 eV are observed in the dielectric function $\varepsilon_2(\hbar\omega)$ for our perovskites. They can be attributed to a threshold to direct optical transitions occurring at about 2.0, 1.36 and 1.0 eV for $KPbI_3$, $LiPbI_3$ and $NaPbI_3$, respectively. Finally, the peaks observed at 5 eV for our perovskites decrease gradually to a minimum at 17 eV.

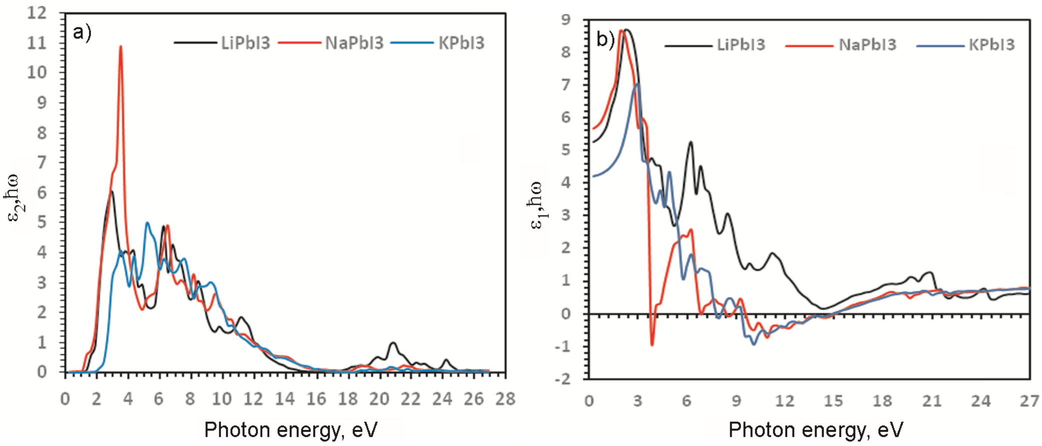

Fig. 8. Imaginary (a) and real (b) parts of the dielectric functions calculated for $MPbI_3$ (M = Li, Na, K).

The real part of the dielectric function is presented in Fig. 8b. The static values calculated for $KPbI_3$, $LiPbI_3$ and $NaPbI_3$ are equal to 4.2, 5.3 and 5.7, respectively. These values correspond to the calculated energy band gaps 1.41494, 1.41336 and 1.39501 eV. In other terms, a compound with a larger band gap energy has a smaller real part of the dielectric function. Fig. 8b demonstrates also that there is a rapid increase in the real part of the dielectric function in the range from 0 to less than 4 eV. It reaches its peaks at about 6.9, 8.53 and 8.65 for $KPbI_3$, $LiPbI_3$ and $NaPbI_3$, respectively.

The peaks in the real parts of the dielectric function observed for the three perovskites are located at less than 4 eV. Beyond this region, the real part of the dielectric permittivity decreases. Larger values of the reflectivity coincide with the region of negativity of the $\varepsilon_1(\hbar\omega)$ function and its maximum occurs at the lowest negative $\varepsilon_1(\hbar\omega)$ value. Negative values of the real part of the dielectric function are experimentally predicted for semiconductors [74]. A negative $\varepsilon_1(\hbar\omega)$ value means that the electric-flux density and the electric field are aligned in the opposite directions. This can occur in the frequency regions where the phase and group velocities are the opposite. Using the spectra calculated for the real (see Eq. (14)) and imaginary (see Eq. (13)) parts of the dielectric function, one can obtain the following spectral dependences of the refractive index n (see Fig. 9) and the extinction coefficient k (see Fig. 10):

$$n = \sqrt{\frac{(\varepsilon_1^2 + \varepsilon_2^2)^{1/2} + \varepsilon_1}{2}}\,, \tag{15}$$

$$k = \sqrt{\frac{(\varepsilon_1^2 + \varepsilon_2^2)^{1/2} - \varepsilon_1}{2}}\,, \quad \alpha = 4\pi\kappa/\lambda_0. \tag{16}$$

The refractive index $n(\omega)$ is an important physical parameter of semiconducting materials [75], which describes light propagation. Comprehensive understanding of the $n(\omega)$ function is crucial for many applications of optical materials, e.g. in the optical devices such as detectors, waveguides, solar cells and photonic crystals [76]. The dependences of $n(\hbar\omega)$ on the photon energy calculated for our perovskites are presented in Fig. 9. Note that a compound with a larger E_g has a smaller refractive index. As seen from Fig. 9, the frequency dependence of the refractive index $n(\omega)$ follows closely that of the $\mathrm{Re}\varepsilon(\omega)$ function (see Fig. 8b). The zero-frequency limits for the refractive index, $n(0)$, are equal to 2.0484, 2.289 and 3.8 respectively for $KPbI_3$, $LiPbI_3$ and $NaPbI_3$.

It is clear from Fig. 9 that the $n(\omega)$ values are high enough for all the three perovskites. High refractive indices in the region 0–4 eV indicate a strong enough interaction of a material with light. The function $n(\omega)$ decreases down to the values less than 0.5 at the energies higher than 13.0 eV and increases slightly in the region 13.5–20.0 eV. The decrease mentioned above shows that there is no essential interaction of light with a material medium. Finally, the refractive index calculated for all of our compounds remains almost the same in the high-energy region 19.5–26.0 eV (see Fig. 9).

The dependences of the absorption coefficient calculated for the $MPbI_3$ (M = Li, Na, K) perovskite on the photon energy are shown in Fig. 10. The absorption edge starts from about 1.36 eV for $NaPbI_3$ and $LiPbI_3$ and from about 2.40 eV for $KPbI_3$. This corresponds to the energy band gaps 1.415, 1.413 and 1.395 eV respectively for $KPbI_3$, $LiPbI_3$ and $NaPbI_3$. The maxima are observed at 9.52 eV for $KPbI_3$, 10.06 eV for $LiPbI_3$ and 11.7 for $NaPbI_3$, thus indicating that our compounds manifest a high enough absorption. Note also that both the first cation and the energy band gap of $MPbI_3$ (M = Li, Na, K) affect somewhat the absorption properties. A high absorption of a material at low photon energies indicates that the material is an appropriate candidate for the solar-cell applications.

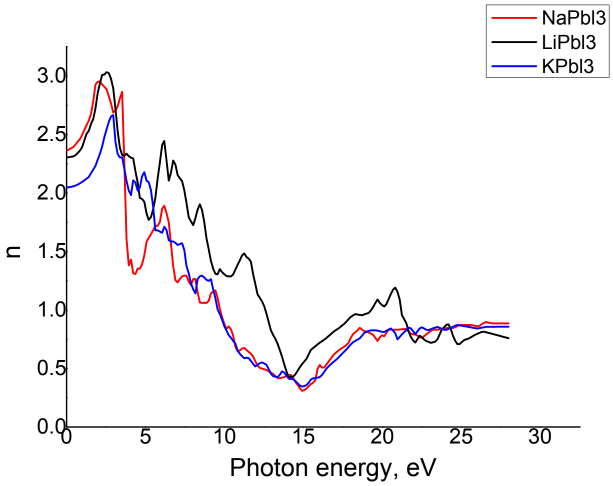

Fig. 9. Refractive indices of $MPbI_3$ (M = Li, Na, K).

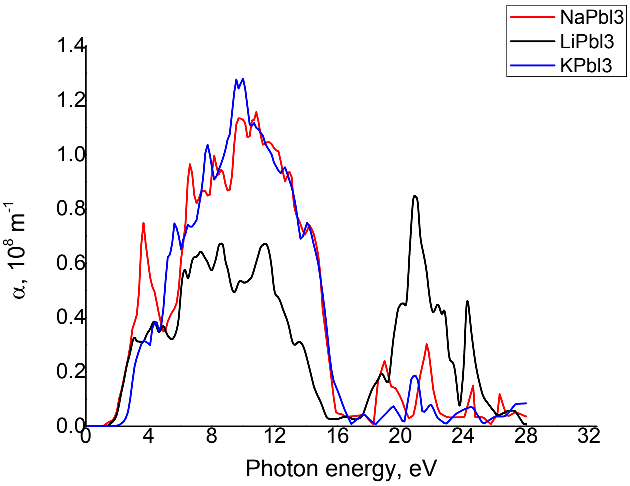

Fig. 10. Absorption coefficients of $MPbI_3$ (M = Li, Na, K).

4. Conclusions

In this work we have investigated the structural, electronics, elastic and optical properties of the $MPbI_3$ (M = Li, Na, K) compounds, using the PBE approach with the GGA exchange-correlation energy and the frame of the density-functional theory. We have also employed the GW approximation as an accurate method for computing the band gap energy. The density-functional perturbation theory with the Kramer–Kronig relations has been implemented to calculate the optical properties of our perovskites.

The Poisson's and Pugh's ratios calculated with the VRH scheme reveal that $LiPbI_3$ is a ductile material. The results obtained by us reveal that the substitution of the first cation in $MPbI_3$ (M = Li, Na, K) does not have a significant effect on the physical properties. It can also be noticed that our compounds reveal a direct fundamental energy band gap located at the symmetry point R. In addition, they manifest a maximal response to the electromagnetic radiation at low photon energies and a minimal response at high energies. Moreover, the wider the fundamental energy gap of $MPbI_3$ (M = Li, Na, K), the smaller its static refractive index and its zero-frequency dielectric function are. The fact of a direct band gap, the band gap value itself and the value of the absorption coefficient calculated for our perovskites testify that they can represent good candidates for various applications in the optoelectronic devices and the solar-cell technologies.

The results derived in the present study agree well with the available experimental and theoretical data. To the best knowledge of the authors, the present work represents the first study of the optical properties of $MPbI_3$ (M = Na, K) and the elastic properties of $MPbI_3$ (M = Li, Na, K). As a future work, it would be interesting to investigate the role of the hydrostatic pressure in tuning the electronic and optical properties of our peroskites.

Acknowledgements. We would like to thank the Ministry of Higher Education & Scientific Research and the University of Zakho for assistance. We also would like to express our great appreciation to the staff of the Physics Department at the University of Zakho for their aid.

Conflict of interest. The authors declare that there is no conflict of interest regarding the publication of this manuscript.

References

1. Stranks S D, Eperon G E, Grancini G, Menelaou C, Alcocer M J, Leijtens T, Herz L M, Petrozza A, Snaith H J and Snaith H J, 2013. Electron-hole diffusion lengths exceeding 1 micrometer in an organometal trihalide perovskite absorber. Science. **342**: 341–344.
2. Burschka J, Pellet N, Moon S J, Humphry-Baker R, Gao P, Nazeeruddin M K and Grätzel M, 2013. Sequential deposition as a route to high-performance perovskite-sensitized solar cells. Nature. **499**: 316–319.
3. Yang W S, Park B W, Jung E H, Jeon N J, Kim Y C, Lee D U, Shin S S, Seo J, Kim E K, Nuh J H and Seok S I, 2017. Iodide management in formamidinium-lead-halide–based perovskite layers for efficient solar cells. Science. **356**: 1376–1379.
4. Duan J, Zhao Y, Yang X, Wang Y, He B and Tang Q, 2018. Lanthanide ions doped $CsPbBr_3$ halides for HTM-free 10.14%-efficiency inorganic perovskite solar cell with an ultrahigh open-circuit voltage of 1.594 V. Adv. Ener. Mater. **8**: 1802346.
5. Kojima A, Teshima K, Shirai Y and Miyasaka T, 2009. Organometal halide perovskites as visible-light sensitizers for photovoltaic cells. J. Amer. Chem. Soc. **131**: 6050–6051.
6. Sahli F, Werner J, Kamino B A, Bräuninger M, Monnard R, Paviet-Salomon B and Ballif C, 2018. Fully textured monolithic perovskite/silicon tandem solar cells with 25.2% power conversion efficiency. Nature Mater. **17**: 820–826.
7. Kim H P, Vasilopoulou M, Ullah H, Bibi S, Gavim A E X, Macedo A G and Nazeeruddin M K, 2020. A hysteresis-free perovskite transistor with exceptional stability through molecular cross-linking and amine-based surface passivation. Nanoscale. **12**: 7641–7650.
8. Yang S, Fu W, Zhang Z, Chen H and Li C Z, 2017. Recent advances in perovskite solar cells: efficiency, stability and lead-free perovskite. J. Mater. Chem. A. **5**: 11462–11482.
9. Sutherland B R and Sargent E H, 2016. Perovskite photonic sources. Nature Photon. **10**: 295–302.
10. Ahmadi M, Wu T and Hu B, 2017. A review on organic–inorganic halide perovskite photodetectors: device engineering and fundamental physics. Adv. Mater. **29**: 1605242.
11. Nazarenko O, Yakunin S, Morad V, Cherniukh I and Kovalenko M V, 2017. Single crystals of caesium formamidinium lead halide perovskites: solution growth and gamma dosimetry. NPG Asia Mater. **9**: e373–e373.
12. Pan Weicheng, Wu Haodi, Luo Jiajun, Deng Zhenzhou, Ge Cong, Chen Chao, Jiang Xiaowei, Yin Wan-Jian, Niu Guangda, Zhu Lujun, Yin Lixiao, Zhou Ying, Xie Qingguo, Ke Xiaoxing, Sui

Manling and Tang Jiang, 2017. $Cs_2AgBiBr_6$ single-crystal X-ray detectors with a low detection limit. Nature Photon. **11**: 726–732.

13. Shockley W and Queisser H J, 1961. Detailed balance limit of efficiency of p-n junction solar cells. J. Appl. Phys. **32**: 510–519.
14. Luo D, Su R, Zhang W, Gong Q and Zhu R, 2020. Minimizing non-radiative recombination losses in perovskite solar cells. Nature Rev. Mater. **5**: 44–60.
15. Duan J, Wang Y, Yang X and Tang Q, 2020. Alkyl-chain-regulated charge transfer in fluorescent inorganic $CsPbBr_3$ perovskite solar cells. Angew. Chem. Int. Ed. **59**: 4391–4395.
16. Grätzel C and Zakeeruddin S M, 2013. Recent trends in mesoscopic solar cells based on molecular and nanopigment light harvesters. Mater. Today. **16**: 11–18.
17. Liu M, Johnston M B and Snaith H J, 2013. Efficient planar heterojunction perovskite solar cells by vapour deposition. Nature. **501**: 395–398.
18. Chen Q, Zhou H, Hong Z, Luo S, Duan H S, Wang H H, Liu Y, Li G and Yang Y, 2014. Planar heterojunction perovskite solar cells via vapor-assisted solution process. J. Amer. Chem. Soc. **136**: 622–625.
19. Jeon N J, Noh J H, Kim Y C, Yang, W S, Ryu S and Seok S I, 2014. Solvent engineering for high-performance inorganic–organic hybrid perovskite solar cells. Nature Mater. **13**: 897–903.
20. Mao X, Sun L, Wu T, Chu T, Deng W and Han K, 2018. First-principles screening of all-inorganic lead-free ABX3 perovskites. J. Phys. Chem. C. **122**: 7670–7675.
21. Wu S, Li Z, Zhang J, Liu T, Zhu Z and Jen A K Y, 2019. Efficient large guanidinium mixed perovskite solar cells with enhanced photovoltage and low energy losses. Chem. Commun. **55**: 4315–4318.
22. Park Y and Park B, 2018. Interfacial energy band bending and carrier trapping at the vacuum-deposited MAPbI3 perovskite/gate dielectric interface. Res. Phys. **11**: 302–305.
23. Tsaytler P, Harding H P, Ron D and Bertolotti A, 2011. Selective inhibition of a regulatory subunit of protein phosphatase 1 restores proteostasis. Science. **332**: 91–94.
24. Brivio F, Walker A B and Walsh A, 2013. Structural and electronic properties of hybrid perovskites for high-efficiency thin-film photovoltaics from first-principles. Appl. Mater. **1**: 042111.
25. Frost J M, Butler K T, Brivio F, Hendon C H, Van Schilfgaarde M and Walsh A, 2014. Atomistic origins of high-performance in hybrid halide perovskite solar cells. Nano Lett. **14**: 2584–2590.
26. Kulbak M, Cahen D and Hodes G, 2015. How important is the organic part of lead halide perovskite photovoltaic cells? Efficient $CsPbBr_3$ cells. J. Phys. Chem. Lett. **6**: 2452–2456.
27. Beal R E, Slotcavage D J, Leijtens T, Bowring A R, Belisle R A, Nguyen W H and McGehee M D, 2016. Cesium lead halide perovskites with improved stability for tandem solar cells. J. Phys. Chem. Lett. **7**: 746–751.
28. Shi J, Wang Y and Zhao Y, 2019. Inorganic $CsPbI_3$ perovskites toward high-efficiency photovoltaics. Energy & Env. Mater. **2**: 73–78.
29. Huang L Y and Lambrecht W R, 2013. Electronic band structure, phonons, and exciton binding energies of halide perovskites $CsSnCl_3$, $CsSnBr_3$, and $CsSnI_3$. Phys. Rev. B. **88**: 165203.
30. Jong U G, Yu C J, Kye Y H, Choe Y G, Hao W and Li S, 2019. First-principles study on structural, electronic, and optical properties of inorganic Ge-based halide perovskites. Inorg. Chem. **58**: 4134–4140.
31. Yapi C M H, Mélèdje C D, Oyédélé O S and Mégnassan E E, 2020. Propriétés électroniques et optiques des pérovskites inorganiques halogénées de type $ASiI_3$ (A= Li, Na, K, Rb et Cs) par la

méthode de la Théorie de la Fonctionnelle de la Densité (DFT). AMReS Sciences des Structures et de la Matière. **2**: 23–34.

32. Dimesso L, Wussler M, Mayer T, Mankel E and Jaegermann W, 2016. Inorganic alkali lead iodide semiconducting $APbI_3$ (A= Li, Na, K, Cs) and NH_4PbI_3 films prepared from solution: structure, morphology, and electronic structure. AIMS Mater. Sci. **3**: 737–755.
33. Abdulkareem N and Sami S, 2019. Structure, bandgap and optical properties of cubic $CsPbX_3$ (X= Cl, Br and I) under hydrostatic pressure. Ukr. J. Phys. Opt. **20**: 132–141.
34. Liang J, Liu J and Jin Z, 2017. All-inorganic halide perovskites for optoelectronics: Progress and prospects. RRL Solar. **1**: 1700086.
35. Ma X, Yang L, Lei K, Zheng S, Chen C and Song H, 2020. Doping in inorganic perovskite for photovoltaic application. Nano Energy. **78**: 105354.
36. Liu C, Li W, Zhang C, Ma Y, Fan J and Mai Y, 2018. All-inorganic $CsPbI_2Br$ perovskite solar cells with high efficiency exceeding 13%. J. Amer. Chem. Soc. **140**: 3825–3828.
37. Wang X, Ran X, Liu X, Gu H, Zuo S, Hui W, Lu H, Sun B, Gao X, Zhang J, Xia Y, Chen Y and Huang W, 2020. Tailoring component interaction for air-processed efficient and stable all-inorganic perovskite photovoltaic. Angew. Chem. Int. Ed. **59**: 13354–13361.
38. Tai Q, Tang K C and Yan F, 2019. Recent progress of inorganic perovskite solar cells. Energy & Environ. Sci. **12**: 2375–2405.
39. Wang Y, Liu X, Zhang T, Wang X, Kan M, Shi J and Zhao Y, 2019. The role of dimethylammonium iodide in $CsPbI_3$ perovskite fabrication: additive or dopant? Angew. Chem. **131**: 16844–16849.
40. Pitriana P, Wungu T D K and Hidayat R, 2019. The characteristics of band structures and crystal binding in all-inorganic perovskite $APbBr_3$ studied by the first principle calculations using the density functional theory (DFT) method. Res. Phys. **15**: 102592.
41. Pitriana P, Wungu T D K, Herman H and Hidayat R, 2019. Electronic structure calculations of alkali lead iodide $APbI_3$ (A= Li, Na, K, Rb or Cs) using density functional theory (DFT) method. J. Phys.: Conf. Ser. **1204**: 012107.
42. Gonze X, Jollet F, Araujo F A, Adams D, Amadon B, Applencourt T, Audouze C, Beuken J-M, Bieder J, Bokhanchukh A, Bousquet E, Bruneval F, Caliste D, Cote M, Dahm F, Da Pieve F, Delaveau M, Di Gennaro M and Zwanziger J W, 2016. Recent developments in the ABINIT software package. Comp. Phys. Commun. **205**: 106–131.
43. Perdew J P, Burke K and Ernzerhof M, 1996. Generalized gradient approximation made simple. Phys. Rev. Lett. **77**: 3865-3868.
44. Krack M, 2005. Pseudopotentials for H to Kr optimized for gradient-corrected exchange-correlation functionals. Theor. Chem. Acc. **114**: 145–152.
45. Goedecker S, Teter M and Hutter J, 1996. Separable dual-space Gaussian pseudopotentials. Phys. Rev. B. **54**: 1703–1710.
46. Monkhorst H J and Pack J D, 1976. Special points for Brillouin-zone integrations. Phys. Rev. B. **13**: 5188.
47. Lucarini V, Saarinen J J, Peiponen K E, Vartiainen E M. Kramers-Kronig Relations in Optical Materials Research. Springer Science & Business Media (2005).
48. Sharma S and Ambrosch-Draxl C, 2004. Second-harmonic optical response from first principles. Phys. Scripta. **2004**: 128–134.
49. Ahmad M, Rehman G, Ali L, Shafiq M, Iqbal R, Ahmad R, Khan T, Jalali-Asadabadi S, Maqbool M and Ahmad I, 2017. Structural, electronic and optical properties of $CsPbX_3$ (X= Cl, Br, I) for

energy storage and hybrid solar cell applications. J. Alloy. Comp. **705**: 828–839.

50. Abdulkareem N A, Sami S A and Elias B H, 2020. Structural, electronic and optical properties of cubic perovskite $CsPbX_3$ (X= Br, Cl and I). Sci. J. Univ. Zakho. **8**: 23–28.
51. Murnaghan F D, 1944. The compressibility of media under extreme pressures. Proc. Natl. Acad. Sci. **30**: 244–247.
52. Birch F, 1947. Finite elastic strain of cubic crystals. Phys.Rev. **71**: 809–824.
53. Belabbas M, Marbouh N, Arbouche O and Hussain A, 2020. Optoelectronic properties of the novel perovskite materials $LiPb(Cl: Br: I)_3$ for enhanced hydrogen production by visible photo-catalytic activity: theoretical prediction based on empirical formulae and DFT. Int. J. Hydrog. Ener. **45**: 33466–33477.
54. Pitriana P, Wungu T D K, Hidayat R and Herman H, 2019. Ab-initio calculation of $APbI_3$ (A= Li, Na, K, Rb and Cs) perovskite crystal and their lattice constants optimization using density functional theory. J. Phys.: Conf. Ser. **1170**: 012023.
55. Pitriana P, Wungu T D K, Herman H and Hidayat R, 2018. The computation parameters optimizations for electronic structure calculation of $LiPbI_3$ perovskite by the density functional theory method. IOP Conf. Ser.: Mater. Sci. Engin. **434**: 012026.
56. Filip M R, Eperon G E, Snaith H J and Giustino F, 2014. Steric engineering of metal-halide perovskites with tunable optical band gaps. Nature Commun. **5**: 1–9.
57. Salau A M, 1980. Fundamental absorption edge in PbI_2: KI alloys. Sol. Ener. Mater. **2**: 327–332.
58. Pugh S F, 1954. XCII. Relations between the elastic moduli and the plastic properties of polycrystalline pure metals. The London, Edinburgh, and Dublin Philos. Mag. J. Sci. **45**: 823–843.
59. Nye J F. Physical Properties of Crystals: Their Representation by Tensors and Matrices. Oxford University Press (1985).
60. Perger W F, Criswell J, Civalleri B and Dovesi R, 2009. Ab-initio calculation of elastic constants of crystalline systems with the CRYSTAL code. Comp. Phys. Commun. **180**: 1753–1759.
61. Pettifor D G, 1992. Theoretical predictions of structure and related properties of intermetallics. Mater. Sci. Techn. **8**: 345–349.
62. Zener C. Elasticity and Anelasticity of Metals. University of Chicago Press (1948).
63. Hill R, 1952. The elastic behaviour of a crystalline aggregate. Proc. Phys. Soc. Sect. A. **65**: 349–354.
64. Born M, 1940. On the stability of crystal lattices. I. Math. Proc. Cambridge Philos. Soc. **36**: 160–172.
65. Liu Y, Hu W C, Li D J, Zeng X Q, Xu C S and Yang X J, 2012. First-principles investigation of structural and electronic properties of $MgCu_2$ Laves phase under pressure. Intermet. **31**: 257–263.
66. Wu Z J, Zhao E J, Xiang H P, Hao X F, Liu X J and Meng J. 2007. Crystal structures and elastic properties of superhard Ir N 2 and Ir N 3 from first principles. Phys. Rev. B. **76**: 054115.
67. Cao J and Li F, 2016. Critical Poisson’s ratio between toughness and brittleness. Philos. Mag. Lett. **96**: 425–431.
68. Liu Z J, Sun X W, Zhang C R, Hu J B, Song T and Qi J H, 2011. Elastic tensor and thermodynamic property of magnesium silicate perovskite from first-principles calculations. Chin. J. Chem. Phys. **24**: 703–710.
69. Liu Y, Wang K, Xiao H, Chen G, Wang Z, Hu T, Fan T and Ma L, 2020. Theoretical study of the mechanical properties of $CrFeCoNiMo_x$ ($0.1 \leq x \leq 0.3$) alloys. RSC Adv. **10**: 14080–14088.
70. Nong Z S, Zhu J C, Cao Y, Yang X W, Lai Z H and Liu Y, 2013. A first-principles study on the structural, elastic and electronic properties of the $C1_4$ Laves phase compounds TiX_2 (X = Cr, Mn, Fe). Physica B. **419**: 11–18.
71. Pfrommer B G, Côté M, Louie S G and Cohen M L, 1997. Relaxation of crystals with the quasi-

Newton method. J. Comp. Phys. **131**: 233–240.

72. Fatima B, Chouhan S S, Acharya N and Sanyal S P, 2014. Structural, electronic, elastic and mechanical properties of ScNi, ScPd and ScPt: a FP-LAPW study. Adv. Mater. Res. **1047**: 27–34.
73. Cohen M L and Chelikowsky J R. Electronic Structure and Optical Properties of Semiconductors (Vol. 75) Springer Science & Business Media (2012).
74. Kumar V, Chandra S and Singh J K, 2017. Electronic, elastic and optical properties of divalent (R+ 2X) and trivalent (R+ 3X) rare earth monochalcogenides. Indian J. Phys. **91**: 875–881.
75. Askari M, Yegnanarayanan S and Adibi A, 2010. Photonic crystal waveguide based refractive index sensor. In Frontiers in Optics 2010 / Laser Science XXVI, OSA Technical Digest (CD) (Optica Publishing Group, 2010), paper FMJ1.
76. Nunes P S, Mortensen N A, Kutter J P and Mogensen K B, 2010. Refractive index sensor based on a 1D photonic crystal in a microfluidic channel. Sensors. **10**: 2348–2358.

Hameed T. Abdulla and Sarkawt A. Sami. 2023. First-principles study of structural, electronic, elastic and optical properties of alkali lead iodides $MPbI_3$ (M = Li, Na, K). Ukr.J.Phys.Opt. **24**: 1 – 21. doi: 10.3116/16091833/24/1/1/2023

Анотація. *Перовськити на основі неорганічних галідів викликають значний інтерес як матеріали для фотоелектричних та оптоелектронних пристроїв. Тут ми представляємо першопринципні дослідження структурних, електронних, пружних і оптичних властивостей йодидів свинцю лужних металів* $MPbI_3$ *(M = Li, Na, K) із наголосом на ролі їхнього першого катіону M. Зокрема, ця робота є першим дослідженням пружних і оптичних властивостей* $MPbI_3$ *(M = Na, K). Наші результати показують, що перший катіон має незначний вплив на згадані вище властивості, хоча спостерігається деяке зростання сталої ґратки при переході від Li до Na. Величини ширини забороненої зони, розраховані для наших перовскітів в узагальненому градієнтному наближенні, узгоджуються з наявними теоретичними даними, але не з експериментальними результатами. Кращої узгодженості з експериментом можна досягти за допомогою підходів функції Гріна та наближення екранованої кулонівської взаємодії. Продемонстровано, що наші сполуки мають пряму заборонену зону. Оптичні властивості* $MP7bI_3$ *розраховано за допомогою теорії збурень функціоналу густини. Наші дані показують, що* $MPbI_3$ *(M = Na, K) виявляють слабку реакцію на електромагнітне випромінювання при високих енергіях фотонів і сильну реакцію при низьких енергіях.*

Ключові слова*: перовськити, структура, пружні властивості, оптичні властивості, теорія функціоналу густини, енергетична щілина, густина станів.*